Formation of hierarchical In2S3–CdIn2S4 heterostructured nanotubes for efficient and stable visible light CO2 reduction

Wang, Sibo; Guan, Bu Yuan; Lu, Yan; Lou, David Xiong Wen

2017

Wang, S., Guan, B. Y., Lu, Y., & Lou, D. X. W. (2017). Formation of hierarchical In2S3–CdIn2S4 heterostructured nanotubes for efficient and stable visible light CO2 reduction. Journal of the American Chemical Society, 139(48), 17305-17308. doi:10.1021/jacs.7b10733

https://hdl.handle.net/10356/137705

https://doi.org/10.1021/jacs.7b10733

Formation of Hierarchical In_2S_3-$CdIn_2S_4$ Heterostructured Nanotubes for Efficient and Stable Visible Light CO_2 Reduction

Sibo Wang, Bu Yuan Guan, Yan Lu, and Xiong Wen (David) Lou*

School of Chemical and Biomedical Engineering, Nanyang Technological University, 62 Nanyang Drive, Singapore 637459, Singapore

Supporting Information Placeholder

ABSTRACT: We demonstrate the rational design and fabrication of hierarchical In_2S_3-$CdIn_2S_4$ heterostructured nanotubes as efficient and stable photocatalysts for visible light CO_2 reduction. The novel self-templated strategy, including sequential anion- and cation-exchange reactions, effectively integrates two distinct sulfide semiconductors into hierarchical tubular hybrids with homogeneous interfacial contacts and ultrathin two-dimensional (2D) nanosheet subunits. Accordingly, the hierarchical heterostructured nanotubes can remarkably facilitate the separation and migration of photoinduced charge carriers, enhance the adsorption and concentration of CO_2 molecules, and offer rich active sites for surface redox reactions. Benefitting from these unique structural and compositional features, the optimized hierarchical In_2S_3-$CdIn_2S_4$ nanotubes without employing any noble metal cocatalysts in the catalytic system manifest remarkable performance for deoxygenative reduction of CO_2 with high CO generation rate (825 μmol h^{-1} g^{-1}) and outstanding stability under visible light irradiation.

Generation of carbon fuels with abundant CO_2 as the feedstock by renewable solar energy is considered as an ideal solution to deal with the global energy and environment challenges.[1-3] Semiconductor-mediated photocatalytic conversion of CO2 to generate value-added products is thus always attracting a lot of attention.[4-13] To date, various semiconductor materials including TiO_2, ZnO, CeO_2, Bi_2WO_6, Ga_2O_3 and $ZnGe_2O_4$ have been reported as photocatalysts for CO_2 reduction.[14-19] Unfortunately, most of these photocatalysts can only response to ultraviolet (UV) light and/or show relatively poor stability upon photoirradiation. Moreover, bulk semiconductors usually exhibit high recombination rate of photogenerated electron-hole pairs. All these drawbacks seriously hamper the efficiency and desired long-term practical application of CO_2 photoreduction. Therefore, the design and construction of visible light-responsive, highly efficient and robust catalysts are of significant importance for photocatalytic CO_2 reduction.

Metal sulfides (e.g., In_2S_3, $ZnIn_2S_4$ and $CdIn_2S_4$) are intriguing visible-light-active photocatalysts with unique electronic structure, tunable optical properties, as well as appropriate band gaps and band edges.[20-27] Meanwhile, the configuration of 2D nanosheets is highly favorable to reduce the diffusion length of charge carriers, provide high surface area and expose abundant catalytically active sites for heterogeneous photocatalysis. Consequently, 2D metal sulfide semiconductors have attracted growing interests in diverse photoredox catalysis, such as photocatalytic H_2 evolution,[20,22] CO_2 photoreduction,[21,26] and organic photosynthesis.[23] Despite these inspiring progresses, the catalytic performance of single metal sulfide photocatalysts is still not satisfactory, mainly due to the sluggish separation and migration kinetics of charge carriers. Heterogeneous coupling of two metal sulfide semiconductors with suitable band gap potentials is expected to be an effective strategy to improve the performance of photocatalysts,[20,23,26,28] because the existence of built-in potential gradient between the nanosized interfaces in the as-obtained photocatalysts can speed up the separation and transfer of electron-hole pairs and ameliorate photostability of the hybrid materials, simultaneously.[20,23,26,28] In addition, the achievement of efficient photocatalytic reactions also relies on the delicate design and fabrication of photocatalysts with proper architectures.

Hollow particles with various constructions and tailored compositions have shown great advantages in diverse research areas.[29-34] Recently, hollow micro/nanostructures are being intensively investigated as powerful light transducers in solar energy-related applications, for example photocatalytic CO_2 reduction, owing to the structure-dependent virtues over their solid counterparties.[15,17,35-40] Specifically, the interior cavity facilitates the separation of charge carriers by decreasing the diffusion length from bulk to surface, offers large surface area to boost CO_2 adsorption and concentration, and promotes surface-dependant redox reactions on both sides of the shell.[15,37-39] Besides, the permeable shells can be precisely modified with cocatalysts and/or additional functional materials to accelerate charge transfer and CO_2 activation at the newly formed interfaces.[15,36,38] Furthermore, the hollow spaces can also enhance photo-harvesting by internal multi-light scattering/reflection.[38,40] Although previous studies on hollow structures for CO_2 photoreduction make some encouraging achievements,[15,37,39] it still remains a great challenge to develop advanced hierarchical hollow structured catalysts with desirable hollow architectures, 2D subunits and heterogeneous compositions for CO_2 photofixation with high efficiency.

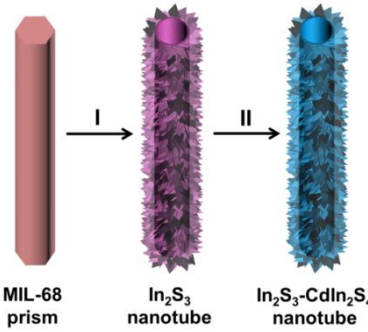

Figure 1. Schematic illustration of the synthetic process of the hierarchical In_2S_3-$CdIn_2S_4$ heterostructured nanotube. (I) liquid phase sulfidation, (II) cation exchange reaction.

Herein, we demonstrate the design and synthesis of hierarchical In_2S_3-$CdIn_2S_4$ heterostructured nanotubes through a novel self-templated strategy for enhanced visible light CO_2 reduction under mild reaction conditions. The overall synthetic strategy for the formation of hierarchical In_2S_3-$CdIn_2S_4$ hybrid nanotubes involves two ion exchange reactions as schematically illustrated in Figure 1. Starting with an In-based MOF (MIL-68) hexagonal prism as the precursor, hierarchical In_2S_3 nanotube is obtained through a liquid phase sulfidation process (step I).[41] Afterward, the as-prepared In_2S_3 tubular nanostructure is controllably transformed into hierarchical In_2S_3-$CdIn_2S_4$ hybrid nanotube through an efficient cation exchange reaction (step II). The developed recipe in this work can realize both the structural and compositional control of the final In_2S_3-$CdIn_2S_4$ hybrid nanotube. When evaluated as a visible light photocatalyst for CO_2 reduction, the optimized In_2S_3-$CdIn_2S_4$ heterostructure exhibits considerable activity and excellent stability for selectively reducing CO_2 into CO without the assistance of any noble metal cocatalysts.

Uniform MIL-68 hexagonal prisms with a high aspect ratio are synthesized *via* a solvothermal reaction of In^{3+} ions with organic ligand 1,4-benzenedicarboxylic acid.[42] Field-emission scanning electron microscopy (FESEM) images show that the average length and diameter of the MIL-68 hexagonal prisms are about 9 μm and 500 nm, respectively (Figure 2a,b). The high-magnification FESEM image clearly reveals the hexagonal prism-shaped morphology of the MIL-68 precursors with smooth surface (Figure 2c). The powder X-ray diffraction (XRD) analysis further demonstrates the formation of In-based MIL-68 (Figure S1).[42] These In-based MOF hexagonal prisms can be easily converted into hierarchical In_2S_3 nanotubes through a liquid phase sulfidation treatment at 180 °C for 3 h. The powder XRD analysis indicates that the MIL-68 precursors are completely converted into cubic In_2S_3 phase (JCPDS card No. 65-0459) without detectable impurities (Figure S2). The energy-dispersive X-ray spectroscopy (EDX) measurement of the In_2S_3 products reveals only In and S elements are detected with a In/S molar ratio of 2: 2.98 (Figure S3), which reaffirms the complete conversion of the In-based MOF precursors into the In_2S_3 phase. FESEM images demonstrate the as-obtained In_2S_3 materials well inherit the one-dimensional (1D) morphology from their MIL-68 precursors with rather rough surface and the average diameter of about 600 nm (Figure 2d,e). The magnified FESEM image shows the surface of the In_2S_3 product is composed of randomly assembled ultrathin nanosheets (Figure 2f). Transmission electron microscopy (TEM) images clearly present the well-defined hierarchical hollow structures of the In_2S_3 nanotubes with the shell thickness of about 100 nm (Figure 2g,h). The elemental mappings of an individual In_2S_3 nanotube show that the S and In elements are uniformly distributed in the whole nanostructure (Figure 2i).

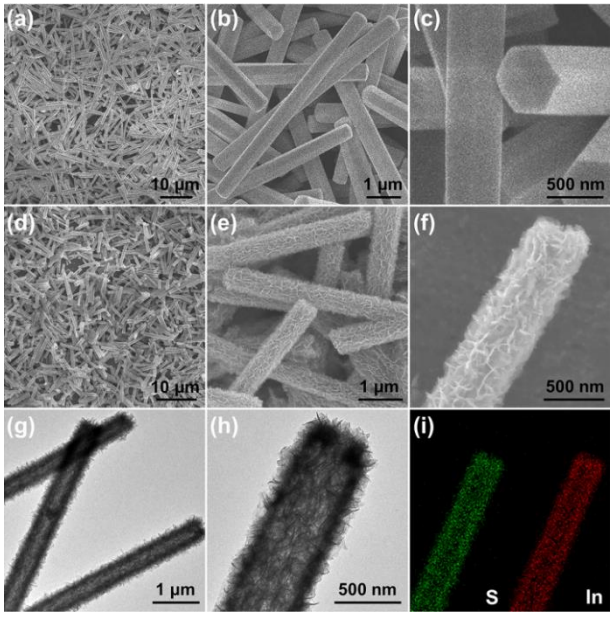

Figure 2. (a-c) FESEM images of MIL-68 hexagonal prisms, (d-f) FESEM and (g,h) TEM images of hierarchical In_2S_3 nanotubes, and (i) elemental mappings of an individual In_2S_3 nanotube.

Then, the as-synthesized In_2S_3 nanotubes are transformed into In_2S_3-$CdIn_2S_4$ hybrids through an efficient hydrothermal cation exchange reaction with Cd^{2+} ions at 60 °C. By controlling the reaction time, the composition of the final composite products can be adjusted. The sample obtained after the ion exchange reaction for 5 min is designated as In_2S_3-$CdIn_2S_4$-5, where the suffix indicates the reaction time in minutes. The EDX analysis reveals that the In_2S_3-$CdIn_2S_4$-5 sample holds a Cd/In molar ratio of 1: 2.72 (Figure S4), suggesting In^{3+} is partially exchanged by Cd^{2+} and the new phase of $CdIn_2S_4$ (JCPDS card No. 31-0229) is generated (Figure S5). Further prolonging the reaction time to 10 min, the fraction of $CdIn_2S_4$ in the In_2S_3-$CdIn_2S_4$-10 sample further increases with the molar ratio of Cd/In increased to 1: 2.31 (Figure S6, also see XRD pattern in Figure S5). When the ion-exchange reaction proceeds for 15 min, the Cd/In molar ratio of the product becomes to be 1: 1.98 (Figure S7), and a pure cubic $CdIn_2S_4$ phase is harvested (Figure S8). The FESEM images demonstrate that the produced In_2S_3-$CdIn_2S_4$ and $CdIn_2S_4$ materials perfectly preserve the overall 1D morphology after the low temperature cation exchange reactions (Figure 3a,b, and Figure S9). Compared with the original In_2S_3 sample, no noticeable changes are observed on the surface of In_2S_3-$CdIn_2S_4$-10 nanotube as revealed by a closer FESEM examination (Figure 3c). TEM images confirm the hierarchical tubular nanostructures of the In_2S_3-$CdIn_2S_4$ and $CdIn_2S_4$ materials (Figure 3d,e, and Figure S10). The magnified side view of a single In_2S_3-$CdIn_2S_4$-10 nanotube indicates

the outmost ultrathin sheet-shaped subunits are unaltered after the ion exchange reaction (Figure 3f). The elemental mappings of a single In_2S_3-$CdIn_2S_4$-10 nanotube show the even distribution of S, In, and Cd elements in the hierarchical nanostructure (Figure 3g), indicating the formation of homogeneous nanosized interfacial contacts between In_2S_3 and $CdIn_2S_4$ nanospecies, which is further revealed by the high-resolution TEM image (Figure S11).

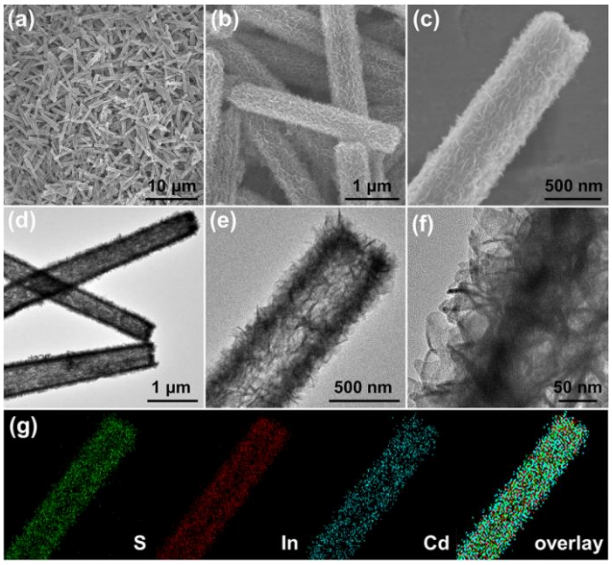

Figure 3. (a-c) FESEM and (d-f) TEM images of hierarchical In_2S_3-$CdIn_2S_4$-10 nanotubes, and (g) elemental mappings of a single In_2S_3-$CdIn_2S_4$-10 nanotube.

To evaluate these hierarchical tubular nanostructures for photocatalytic applications, the optical absorption properties and band gap energies of the materials are investigated by UV-Vis diffuse reflectance spectroscopy (DRS). The results show that the In_2S_3, In_2S_3-$CdIn_2S_4$-5, In_2S_3-$CdIn_2S_4$-10 and $CdIn_2S_4$ samples exhibit strong optical absorption extending to the visible light region (Figure S12). Their band gap energies are calculated to be 2.15, 2.18, 2.21 and 2.22 eV respectively from the corresponding Tauc plots (Figure S13), which are similar to the reported values.[22,24] Such findings confirm that these materials can be excited by visible light irradiation to generate electron-hole pairs for redox reactions. Furthermore, the conduction bands (CB) of the materials are determined by the Mott-Schottky plots. The derived flat-band potentials of the In_2S_3, In_2S_3-$CdIn_2S_4$-5, In_2S_3-$CdIn_2S_4$-10 and $CdIn_2S_4$ samples are about -0.73, -0.95, -1.03, and -1.13 V (*vs.* normal hydrogen electrode, NHE, pH = 7.0, Figure S14), which ensures their appropriate redox potentials to manipulate CO2 reduction reactions.[3] The N_2 adsorption-desorption measurement reveals that the hierarchical In_2S_3-$CdIn_2S_4$-10 nanotubes possess a high BET surface area of 68 $m^2\ g^{-1}$. The N_2 sorption isotherm processes a hysteresis loop (Figure S15), indicating the existence of mesopores in the hierarchical structure. The advantage of such porous characteristics for improving CO_2 adsorption and concentration is further demonstrated by CO_2 adsorption measurements. The result reveals that the hierarchical nanotubes exhibit a high CO_2 uptake of *ca.* 25 $cm^3\ g^{-1}$ at 760 mmHg and 0 °C (Figure S16). In addition, the presence of mesopores can offer more catalytically active sites and accelerate mass/charge transfer to promote photoredox catalysis.

The separation-recombination rate of photogenerated charge carriers of these hybrid materials is estimated by room temperature photoluminescence (PL) characterization. Results demonstrate that the In_2S_3-$CdIn_2S_4$-10 sample exhibits a remarkable fluorescence quenching compared with the In_2S_3 and $CdIn_2S_4$ samples (Figure S17). This observation in principle indicates the greatly inhibited electron-hole recombination in the heterostructured material,[21] which is favorable for heterogeneous photocatalysis. On the other hand, the evidently enhanced photocurrent density generated on the In_2S_3-$CdIn_2S_4$-10 sample strongly illustrates the promoted transfer kinetics of photoexcited charge carriers (Figure S18). These photoelectrochemical characterizations provide solid proofs that the In_2S_3-$CdIn_2S_4$-10 hybrid material possesses enhanced separation and migration of photoinduced charge carriers, which is attributed to the unique heterogeneous composition and hierarchical structure of the In_2S_3-$CdIn_2S_4$ nanotubes.

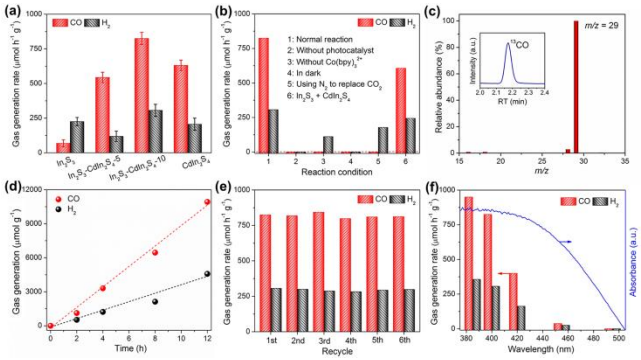

Figure 4. Performance of In_2S_3-$CdIn_2S_4$-10 nanotubes for CO_2 photoreduction. (a) Generation of CO and H_2 over different samples. (b) Evolution of CO and H_2 under various reaction conditions. (c) Results of GC-MS analysis for CO produced from $^{13}CO_2$ isotope experiment. (d) Production of CO and H_2 as a function of reaction time. (e) Formation of CO and H_2 in stability tests. (f) Wavelength dependence of yields of CO and H_2, and the light absorption spectrum of In_2S_3-$CdIn_2S_4$-10 photocatalyst.

The photocatalytic CO_2 reduction performance of the In_2S_3-$CdIn_2S_4$ heterostructured materials is evaluated in a tandem catalytic system conducted in H_2O/acetonitrile mixture with $Co(bpy)_3^{2+}$ (bpy = 2'2-bipyridine) and triethanolamine (TEOA) as the cocatalyst and electron donor, respectively, under visible light irradiation and mild conditions ($\lambda \geq 400$ nm, 30 °C, 1 atm CO_2).[10,43] Figure 4a shows the performance of CO_2 reduction reactions with different samples as the photocatalysts. The pure In_2S_3 sample only exhibits moderate activity for deoxygenative CO_2 reduction with a CO generation rate of 68 $\mu mol\ h^{-1}\ g^{-1}$. Once the In_2S_3-$CdIn_2S_4$ heterostructures are employed, the CO_2 reduction performance is substantially improved. In particular, the In_2S_3-$CdIn_2S_4$-10 sample manifests the highest CO production rate of 825 $\mu mol\ h^{-1}\ g^{-1}$, which is about 12 times higher than that of the In_2S_3 material. The achieved CO_2 reduction rate is fairly comparable to some noble-metal-containing CO_2 conversion systems (Table S1).[5-9] When using $CdIn_2S_4$ as the photocatalyst, the catalytic system displays much decreased activity. These observations highlight the remarkable CO_2 photoreduction performance of the

In_2S_3-$CdIn_2S_4$-10 hybrid material. The main reason might be that the unique structural and compositional features of the hierarchical nanotubes facilitate the separation and mobility of charge carriers. No detectable liquid products (e.g., HCOOH, CH_3OH and CH_3CH_2OH) are generated in the reaction system, consistent with results of reported works.[10,43]

Furthermore, the CO_2-to-CO conversion reaction stops completely without the addition of In_2S_3-$CdIn_2S_4$-10 photocatalyst in the catalytic system (Figure 4b, column 2). Meanwhile, the cocatalyst of $Co(bpy)_3^{2+}$ is indispensable to realize efficient CO_2 reduction performance (Figure 4b, column 3).[10,43] Besides, no products are produced in dark, suggesting the photocatalytic nature of the CO_2 conversion reaction (Figure 4b, column 4). When the CO_2 reactant is replaced by N_2 under otherwise identical conditions, the reaction system only generates a small amount of H_2, and no CO is detected (Figure 4b, column 5). This observation indicates the produced CO stems from the CO_2 feedstock. To provide direct proof for the carbon source of evolved CO, ^{13}C-isotopic tracer experiments are carried out. Results of gas chromatography-mass spectrometer (GC-MS) analysis reveal only ^{13}CO is detected when using $^{13}CO_2$ as the gas source (Figure 4c), which is a strong evidence that the produced CO is originated from photocatalytic reduction of CO_2 molecules. In addition, the physical mixture of In_2S_3 and $CdIn_2S_4$ shows much inferior CO_2 reduction activity compared to the In_2S_3-$CdIn_2S_4$-10 composite (Figure 4b, column 6), indicating the formation of heterostructures in the latter is favorable for photocatalytic CO_2 conversion.

The time-yield plots of the products are illustrated in Figure 4d. The generation of CO/H_2 increases almost linearly with reaction time and no apparent loss in the reaction rate is noticed after photoreaction for 12 h, reflecting the high stability of the In_2S_3-$CdIn_2S_4$-10 photocatalyst. During the catalytic reaction, the accumulated formation of products is *ca.* 1.55×10^4 μmol g^{-1}. To further examine its stability, the In_2S_3-$CdIn_2S_4$-10 photocatalyst is repeatedly used to operate the CO_2-to-CO conversion reactions for 24 h and the generation rates of the products in every 4 h reaction are determined. As shown in Figure 4e, no evident deactivation with time is found in the tests of 6 cycles. These findings underline the excellent stability of the In_2S_3-$CdIn_2S_4$-10 hybrid photocatalyst, which is quite different from many other single metal sulfide photocatalysts which usually suffer from photocorrosion.[20,26,44] Moreover, XRD and FESEM characterizations of used In_2S_3-$CdIn_2S_4$-10 after photocatalysis also support the high stability of the hybrid material (Figure S19 and S20). Performance of CO_2 photoreduction reactions is also investigated by light irradiation with different wavelengths. The trend of CO/H_2 evolution rate is in good agreement with the optical absorption spectrum of the In_2S_3-$CdIn_2S_4$-10 material (Figure 4f). This observation reveals that the CO_2 reduction reaction is triggered by photo-excitation of the In_2S_3-$CdIn_2S_4$-10 catalyst to achieve charge generation, separation and subsequent tandem electron transfer catalysis.

In summary, hierarchical In_2S_3-$CdIn_2S_4$ heterostructured nanotubes are synthesized through a self-templated strategy as efficient and stable photocatalysts for CO_2 reduction with visible light. The developed strategy, including sequential ion exchange reactions, can realize both structural and compositional control of the final hybrid materials. These hierarchical tubular nanostructures hold unique structural and compositional features, such as nanosized interfacial contacts, reduced diffusion length for charge carriers separation and migration, large surface area for CO_2 adsorption and concentration, and rich catalytically active sites for photochemical reactions. Consequently, the optimized In_2S_3-$CdIn_2S_4$ hybrid photocatalyst exhibits remarkable performance for deoxygenative CO_2 reduction with high CO generation rate and outstanding stability under visible light irradiation. This work may provide some guidelines for the design and construction of complex semiconductor-based photocatalysts for solar energy-related applications.

ASSOCIATED CONTENT

Supporting Information

The experimental details, more FESEM/TEM images, XRD, EDX, DRS, Tauc plots, Mott-Schottky plots, N_2 adsorption isotherms, CO_2 sorption isotherms, PL spectra, and transient photocurrent response. This material is available free of charge *via* the Internet at http://pubs.acs.org.

AUTHOR INFORMATION

Corresponding Author

Email: xwlou@ntu.edu.sg;

Notes

The authors declare no competing financial interests.

ACKNOWLEDGEMENTS

X. W. L. acknowledges the funding support from the National Research Foundation (NRF) of Singapore via the NRF investigatorship (NRF-NRFI2016-04).

REFERENCES

(1) Listorti, A.; Durrant, J.; Barber, J. *Nat. Mater.* **2009**, *8*, 929.
(2) Lewis, N. S.; Nocera, D. G. *Proc. Natl. Acad. Sci. USA* **2006**, *103*, 15729.
(3) Schneider, J.; Jia, H.; Muckerman, J. T.; Fujita, E. *Chem. Soc. Rev.* **2012**, *41*, 2036.
(4) Wang, S.; Yao, W.; Lin, J.; Ding, Z.; Wang, X. *Angew. Chem. Int. Ed.* **2014**, *53*, 1034.
(5) Sato, S.; Morikawa, T.; Saeki, S.; Kajino, T.; Motohiro, T. *Angew. Chem. Int. Ed.* **2010**, *49*, 5101.
(6) Kuriki, R.; Matsunaga, H.; Nakashima, T.; Wada, K.; Yamakata, A.; Ishitani, O.; Maeda, K. *J. Am. Chem. Soc.* **2016**, *138*, 5159.
(7) Kuriki, R.; Yamamoto, M.; Higuchi, K.; Yamamoto, Y.; Akatsuka, M.; Lu, D.; Yagi, S.; Yoshida, T.; Ishitani, O.; Maeda, K. *Angew. Chem. Int. Ed.* **2017**, *56*, 4867.
(8) Kang, Q.; Wang, T.; Li, P.; Liu, L.; Chang, K.; Li, M.; Ye, J. *Angew. Chem. Int. Ed.* **2015**, *54*, 841.
(9) Gao, C.; Meng, Q.; Zhao, K.; Yin, H.; Wang, D.; Guo, J.; Zhao, S.; Chang, L.; He, M.; Li, Q.; Zhao, H.; Huang, X.; Guo, Y.; Tang, Z. *Adv. Mater.* **2016**, *28*, 6485.
(10) Lin, J.; Pan, Z.; Wang, X. *ACS Sustainable Chem. Eng.* **2013**, *2*, 353.
(11) Shi, L.; Wang, T.; Zhang, H.; Chang, K.; Ye, J. *Adv. Funct. Mater.* **2015**, *25*, 5360.
(12) Fu, Y.; Sun, D.; Chen, Y.; Huang, R.; Ding, Z.; Fu, X.; Li, Z. *Angew. Chem. Int. Ed.* **2012**, *51*, 3364.

(13) Xu, H. Q.; Hu, J.; Wang, D.; Li, Z.; Zhang, Q.; Luo, Y.; Yu, S. H.; Jiang, H. L. *J. Am. Chem. Soc.* **2015**, *137*, 13440.
(14) Inoue, T.; Fujishima, A.; Konishi, S.; Honda, K. *Nature* **1979**, *277*, 637.
(15) Cheng, H.; Huang, B.; Liu, Y.; Wang, Z.; Qin, X.; Zhang, X.; Dai, Y. *Chem. Commun.* **2012**, *48*, 9729.
(16) Liu, Q.; Zhou, Y.; Kou, J.; Chen, X.; Tian, Z.; Gao, J.; Yan, S.; Zou, Z. *J. Am. Chem. Soc.* **2010**, *132*, 14385.
(17) Liu, S.; Yu, J.; Jaroniec, M. *J. Am. Chem. Soc.* **2010**, *132*, 11914.
(18) Habisreutinger, S. N.; Schmidt-Mende, L.; Stolarczyk, J. K. *Angew. Chem. Int. Ed.* **2013**, *52*, 7372
(19) Li, P.; Zhou, Y.; Zhao, Z.; Xu, Q.; Wang, X.; Xiao, M.; Zou, Z. *J. Am. Chem. Soc.* **2015**, *137*, 9547.
(20) Iwashina, K.; Iwase, A.; Ng, Y. H.; Amal, R.; Kudo, A. *J. Am. Chem. Soc.* **2015**, *137*, 604.
(21) Jiao, X.; Chen, Z.; Li, X.; Sun, Y.; Gao, S.; Yan, W.; Wang, C.; Zhang, Q.; Lin, Y.; Luo, Y.; Xie, Y. *J. Am. Chem. Soc.* **2017**, *139*, 7586.
(22) Kale, B. B.; Baeg, J. O.; Lee, S. M.; Chang, H.; Moon, S. J.; Lee, C. W. *Adv. Funct. Mater.* **2006**, *16*, 1349.
(23) Chen, W.; Hua, Y. X.; Wang, Y.; Huang, T.; Liu, T. Y.; Liu, X. H. *J. Catal.* **2017**, *349*, 8.
(24) Batabyal, S. K.; Lu, S. E.; Vittal, J. J. *Cryst. Growth Des.* **2016**, *16*, 2231.
(25) Apte, S. K.; Garaje, S. N.; Bolade, R. D.; Ambekar, J. D.; Kulkarni, M. V.; Naik, S. D.; Gosavi, S. W.; Baeg, J. O.; Kale, B. B. *J. Mater. Chem.* **2010**, *20*, 6095.
(26) Iwase, A.; Yoshino, S.; Takayama, T.; Ng, Y. H.; Amal, R.; Kudo, A. *J. Am. Chem. Soc.* **2016**, *138*, 10260.
(27) Gou, X.; Cheng, F.; Shi, Y.; Zhang, L.; Peng, S.; Chen, J.; Shen, P. *J. Am. Chem. Soc.* **2006**, *128*, 7222.
(28) Wang, H.; Zhang, L.; Chen, Z.; Hu, J.; Li, S.; Wang, Z.; Liu, J.; Wang, X. *Chem. Soc. Rev.* **2014**, *43*, 5234.
(29) Yu, L.; Wu, H. B.; Lou, X. W. *Acc. Chem. Res.* **2017**, *50*, 293.
(30) Guan, B. Y.; Yu, L.; Li, J.; Lou, X. W. *Sci. Adv.* **2016**, *2*, e1501554.
(31) Lai, X.; Halpert, J. E.; Wang, D. *Energy Environ. Sci.* **2012**, *5*, 5604.
(32) Wang, S.; Guan, B. Y.; Yu, L.; Lou, X. W. *Adv. Mater.* **2017**, *29*, 1702724.
(33) Guan, B. Y.; Yu, X. Y.; Wu, H. B.; Lou, X. W. *Adv. Mater.* **2017**, DOI: 10.1002/adma.201703614.
(34) Guan, B. Y.; Yu, L.; Lou, X. W. *Angew. Chem. Int. Ed.* **2017**, *56*, 2386.
(35) Zhu, T.; Wu, H. B.; Wang, Y.; Xu, R.; Lou, X. W. *Adv. Energy Mater.* **2012**, *2*, 1497.
(36) Zheng, D.; Cao, X. N.; Wang, X. *Angew. Chem. Int. Ed.* **2016**, *55*, 11512.
(37) Tu, W.; Zhou, Y.; Liu, Q.; Tian, Z.; Gao, J.; Chen, X.; Zhang, H.; Liu, J.; Zou, Z. *Adv. Funct. Mater.* **2012**, *22*, 1215.
(38) Sun, J.; Zhang, J.; Zhang, M.; Antonietti, M.; Fu, X.; Wang, X. *Nat. Commun.* **2012**, *3*, 1139.
(39) In, S. I.; Vaughn, D. D.; Schaak, R. E. *Angew. Chem. Int. Ed.* **2012**, *51*, 3915.
(40) Qiu, B.; Zhu, Q.; Du, M.; Fan, L.; Xing, M.; Zhang, J. *Angew. Chem. Int. Ed.* **2017**, *56*, 2684.
(41) Zhang, H.; Nai, J.; Yu, L.; Lou, X. W. *Joule* **2017**, *1*, 77.
(42) Cho, W.; Lee, H. J.; Oh, M. *J. Am. Chem. Soc.* **2008**, *130*, 16943.
(43) Qin, J.; Wang, S.; Ren, H.; Hou, Y.; Wang, X. *Appl. Catal. B: Environ.* **2015**, *179*, 1.
(44) Kuehnel, M. F.; Orchard, K. L.; Dalle, K. E.; Reisner, E. *J. Am. Chem. Soc.* **2017**, *139*, 7217.

TOC graphic

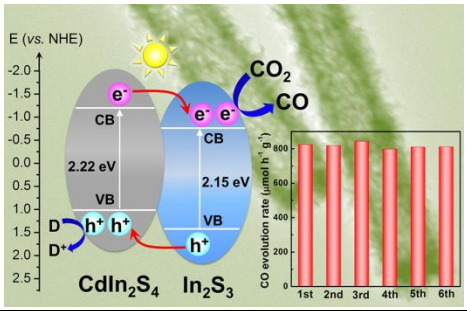
E (vs. NHE)
-2.0
-1.5
-1.0
-0.5
0.0
0.5
1.0
1.5
2.0
2.5
e⁻
CB
2.22 eV
VB
D
D⁺
h⁺ h⁺
CdIn2S4
e⁻ e⁻
CO2
CO
CB
2.15 eV
VB
h⁺
In2S3
CO evolution rate (μmol h⁻¹ g⁻¹)
800
600
400
200
0
1st 2nd 3rd 4th 5th 6th